

Dynamical tunneling with ultracold atoms in magnetic microtraps

Martin Lenz,^{1,2,*} Sebastian Wüster,^{1,3} Christopher J. Vale,^{1,4} Norman R. Heckenberg,¹ Halina Rubinsztein-Dunlop,¹ C. A. Holmes,¹ G. J. Milburn,¹ and Matthew J. Davis^{1,†}

¹The University of Queensland, School of Mathematics and Physics, Brisbane, Queensland 4072, Australia

²University Paris Sud, CNRS, LPTMS, UMR 8626, Orsay 91405, France

³Max Planck Institute for the Physics of Complex Systems, Nöthnitzer Strasse 38, 01187 Dresden, Germany

⁴ARC Centre of Excellence for Quantum-Atom Optics and Centre for Atom Optics and Ultrafast Spectroscopy, Swinburne University of Technology, Melbourne, Victoria 3122, Australia

(Received 25 March 2013; published 29 July 2013)

The study of dynamical tunneling in a periodically driven anharmonic potential probes the quantum-classical transition via the experimental control of the effective Planck's constant for the system. In this paper we consider the prospects for observing dynamical tunneling with ultracold atoms in magnetic microtraps on atom chips. We outline the driven anharmonic potentials that are possible using standard magnetic traps and find the Floquet spectrum for one of these as a function of the potential strength, modulation, and effective Planck's constant. We develop an integrable approximation to the nonintegrable Hamiltonian and find that it can explain the behavior of the tunneling rate as a function of the effective Planck's constant in the regular region of parameter space. In the chaotic region we compare our results with the predictions of models that describe chaos-assisted tunneling. Finally, we examine the practicality of performing these experiments in the laboratory with Bose-Einstein condensates.

DOI: [10.1103/PhysRevA.88.013635](https://doi.org/10.1103/PhysRevA.88.013635)

PACS number(s): 03.75.Lm, 05.45.Mt, 03.65.Xp

I. INTRODUCTION

Tunnelling is one of the ubiquitous features of wave mechanics. A familiar example of quantum tunneling of a single particle occurs in a time-independent spatially symmetric double-well potential. A quantum particle initially located in one of the wells with an energy below the maximum of the potential barrier between the wells will tunnel between them, despite this being classically forbidden (see, for instance, Ref. [1]). However, tunnelling is a more general phenomenon that can be observed in situations involving other types of symmetries and barriers.

In this paper we are interested in dynamical tunneling in classically nonintegrable systems, i.e., Hamiltonian systems with more degrees of freedom than constants of motion. The classical dynamics of such systems is known to exhibit chaotic features [2]. However, for a Hamiltonian of the form $H_0 + \epsilon V$, where H_0 is integrable and ϵV is a sufficiently small chaos-inducing perturbation (a quasi-integrable system), some constants of motion are locally conserved, leading to the formation of so-called Kolmogorov-Arnol'd-Moser (KAM) tori [2]. Within these tori the dynamics of the system is still regular. Poincaré surfaces of sections of such systems show characteristic patterns of seas of chaos surrounding islands of regular motion [see, for instance, Fig. 1(d)].

While particles cannot classically escape the regions bound by the KAM tori, quantum mechanical particles are able to tunnel through KAM barriers to symmetry-related islands [3]. Due to the similarities with spatial tunneling in double wells and the dynamical origin of the barrier the quantum particle crosses, this phenomenon was named *dynamical tunnelling* by Davis and Heller [4].

Laser-cooled atomic gases confined in magneto-optical traps have proven to be useful systems for the demonstration of single-particle matter wave phenomena. Impressive examples include Kapitza-Dirac scattering [5], Bragg scattering [6], two-slit interference [7], and Wannier-Stark ladders [8]. One of the first experimental demonstrations of dynamical tunneling by Steck *et al.* began with velocity-selected cold atoms from a magneto-optical trap [9].

Further decreasing the temperature of cold-atom systems via evaporative cooling can lead to the formation of a Bose-Einstein condensate (BEC)—a “giant” matter wave. This can lead to practical advantages in studying the physics of matter waves, as the increase in phase-space density combined with macroscopic coherence allows for the single shot visualization of single-particle matter wave phenomena, such as interference [10] and quantum tunneling [11]. However, the repulsive interactions common in atomic BEC can cause additional complications. A second experimental demonstration of dynamical tunneling by Hensinger *et al.* used a Bose-Einstein condensate as their starting point [12]. The BEC was released from its initial trap, and allowed to expand until the interaction energy was negligible. Single-particle dynamical tunneling was observed in the following dynamics [13]. Another recent experiment on dynamical tunneling succeeded in extracting the full phase-space representation of the quantum state of a kicked top [14,15].

A common theoretical model for dynamical tunneling is that of the nonlinear pendulum, with the dimensionless Hamiltonian

$$H = \frac{p^2}{2} + \kappa(1 + 2\epsilon \cos t) \sin^2\left(\frac{q}{2}\right), \quad (1)$$

where p , q , and t are the dimensionless momentum, position, and time variables, respectively; κ is the potential strength; and ϵ is the strength of the driving. This potential can be

*martin.lenz@u-psud.fr

†mdavis@physics.uq.edu.au

realized experimentally with cold atoms placed in an intensity modulated optical standing wave, and this was the system realized by Steck *et al.* [9] and Hensinger *et al.* [12].

One of the motivations for the theoretical study of dynamical tunneling has been to explore the boundary between classical and quantum dynamics. The relevant parameter is the effective Planck's constant, defined by the commutator $[\hat{q}, \hat{p}] = i\hbar_{\text{eff}}$ of the dimensionless position q and momentum p variables of the Hamiltonian, Eq. (1). By varying experimental parameters it is in principle feasible to carry out experiments that are identical apart from differing values of \hbar_{eff} . This would, for example, lead to a variation in the rate of tunnelling, and this has been studied in a large number of theoretical papers [16–26]. However, the experiments performed by Steck *et al.* [9] and Hensinger *et al.* [12] considered single, large values of \hbar_{eff} , and, while impressive, they did not probe the quantum-classical transition that occurs as $\hbar_{\text{eff}} \rightarrow 0$. Here we revisit the problem of observing dynamical tunneling in an experiment with ultracold atoms for a range of effective Planck's constant \hbar_{eff} to probe the quantum-classical transition.

As well as working at large \hbar_{eff} , the modulated standing-wave potential for cold atoms used in Refs. [9,12] to study dynamical tunneling does not directly correspond to the classical nonlinear pendulum. The phase space of the pendulum has periodic boundary conditions for the position variable, while atoms in an optical standing wave can move between lattice sites. The value of \hbar_{eff} used by Hensinger *et al.* [12] was sufficiently large that during the dynamics the atoms were not confined to a single well of the standing wave [12,13,27]. Thus, the Husimi functions of the tunneling Floquet states were not confined to a single lattice site, and long-range coherence played an important role in the observed dynamics [12,13,27]. This complicates the picture that was presented in Ref. [12] of a classical particle tunneling to an oscillatory mode with the same amplitude but 180° out of phase. One way of avoiding this would be to use a trapping potential with a single minimum rather than multiple minima. Then, within the approximation that all atoms share the same single-particle wave function, all atoms will experience the same dynamics.

For a one-dimensional system, a sinusoidal modulation of the trapping potential can lead to a mixed phase space with symmetric islands of regular motion. If the potential is anharmonic then dynamical tunneling may occur between the period-one islands in the phase space. However, to a first approximation almost all ultracold atom experiments occur in harmonic trapping potentials. One possible realization of an anharmonic potential for ultracold atoms is the radial trapping potential formed by the magnetic field from current-carrying microscopic wires combined with a homogeneous bias field on an atom chip [28]. While such potentials are harmonic at the center, beyond a certain length scale they become linear. Also, these microtraps can be made very tight, potentially giving access to a large range of \hbar_{eff} , a crucial prerequisite for studies of the quantum-classical transition and so far not achieved in cold atom experiments.

While quantum chaos and dynamical tunneling are purely single-particle effects, the preparation of a BEC greatly simplifies the efficient loading of small regions of phase space. Therefore, in this paper we consider the possibilities for studies of quantum chaos using BECs confined by magnetic potentials

on an atom chip. As long as the condensate is sufficiently dilute, its dynamical tunneling is to a good approximation dominated by single-particle physics, to which we devote a large part of this article. We outline our model in Sec. II, before describing our numerical results for dynamical tunneling in a 1D atom-chip potential in Sec. III. We analyze these results using different theoretical methods and, in particular, derive an integrable approximation that explains some of the observed features. In Sec. IV we consider the practicalities of realizing these experiments, including the effect of mean-field interactions in the BEC, before concluding in Sec. V. In Appendix A we outline the derivation of the possible potentials realizable with an atom chip, essentially consisting of an infinite wire carrying a time-dependent current combined with a time-dependent bias magnetic field. In Appendix B we derive the reduced dimensional Gross-Pitaevskii equation that we use for simulations in Sec. IV.

II. MODEL

A. Hamiltonian

We consider a time-dependent potential realized by a current-carrying wire and a homogeneous bias magnetic field. Reducing the problem to one dimension and making use of dimensionless units (see Appendix A), the following dimensionless Hamiltonian can be realized:

$$H_m = \frac{p^2}{2} + \kappa(1 + \epsilon \cos t)(1 + q^2)^{1/2}. \quad (2)$$

Here the dimensionless momentum p , position q , and time t variables can be converted to SI units by multiplying by the quantities

$$\bar{p} = \frac{B_0 m \Omega}{B'}, \quad \bar{q} = \frac{B_0}{B'}, \quad \bar{t} = \frac{1}{\Omega}, \quad (3)$$

respectively. Here B' is the magnetic field gradient at the trap center, B_0 is the magnetic field offset, Ω is the frequency of modulation of the trapping potential, and m is the mass of the atom. The amplitude of the driving potential is given by ϵ , and the strength of the potential is

$$\kappa = \frac{g m_F \mu_B B^2}{m B_0 \Omega^2} \equiv \frac{\omega_r^2}{\Omega^2}, \quad (4)$$

where g is the Landé g factor, m_F identifies the magnetic sublevel of the atom, μ_B is the Bohr magneton, and ω_r is the harmonic trapping frequency about the minimum of the potential for small amplitude oscillations. A detailed derivation of the Hamiltonian Eq. (2) can be found in Appendix A.

B. Classical dynamics

The parameters κ and ϵ are experimentally tunable, and altering them allows the investigation of various dynamical regimes. Example Poincaré sections for two values of κ and ϵ are shown in Fig. 1.

In this article we consider the dynamics associated with the fixed points resulting from the 1:1 resonance of the unperturbed motion (described by $H_0 = p^2/2 + \kappa\sqrt{1+q^2}$) with the period of the perturbation $\epsilon V = \epsilon\kappa \cos t \sqrt{1+q^2}$. As the quantity κ is increased from zero, two such fixed points

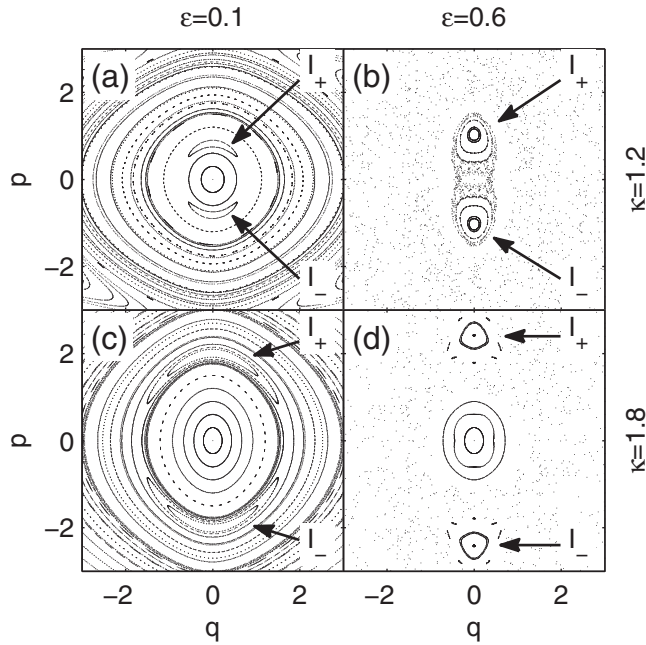


FIG. 1. Poincaré sections for the classical dynamics of the atom-chip Hamiltonian, Eq. (2) at $t = 0$, illustrating the influence of the potential strength κ and modulation amplitude ϵ on the classical dynamics. We show results for the parameters: (a) $\kappa = 1.2$, $\epsilon = 0.1$; (b) $\kappa = 1.2$, $\epsilon = 0.6$; (c) $\kappa = 1.8$, $\epsilon = 0.1$; (d) $\kappa = 1.8$, $\epsilon = 0.6$.

appear at the origin of the phase space at $\kappa = 1$ [29] and then move away from each other, as plotted in Fig. 2.

As ϵ is increased, the KAM tori constraining the motion to regular behavior are progressively destroyed, and larger regions of chaos appear about the islands centered on the period-one resonances.

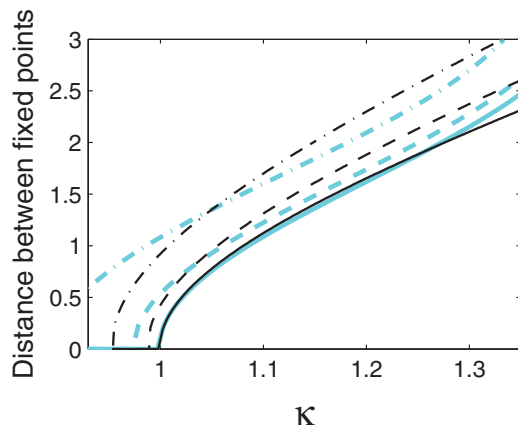


FIG. 2. (Color online) Distance in phase-space between the period-one resonances at $t = 0$ as a function of potential strength κ for three values of modulation strength ϵ . The black curves are determined from the Poincaré section for the full Hamiltonian Eq. (2). The cyan (gray) curves are the corresponding result derived from the integrable approximation to the full Hamiltonian, Eq. (9), as introduced in Sec. III B. These give an indication of the validity of the integrable approximation. Solid lines: $\epsilon = 0.1$. Dashed lines: $\epsilon = 0.4$. Dash-dot lines: $\epsilon = 0.8$.

C. Quantum dynamics

The effective Planck's constant for this system is the commutator of the dimensionless quantum position and momentum operators,

$$\hbar_{\text{eff}} = i[\hat{p}, \hat{q}] = \frac{\hbar B^2}{B_0^2 m \Omega}. \quad (5)$$

Larger values of \hbar_{eff} correspond to systems that are “more quantum.” It is possible to experimentally tune this parameter while retaining fixed values of κ and ϵ .

In a quantum system, dynamical tunneling will take place between the period-one islands of regular motion \mathcal{I}_+ and \mathcal{I}_- of the classical Hamiltonian because of their time-reversal symmetry. This can be understood using Floquet theory, a formalism used to describe systems with a periodic time dependence [3,9,12,17–21,30–32]. The Floquet operator \hat{F} describes quantum evolution for one period of the potential modulation, T_0 , and its eigenstates are invariant under a $T_0 = 2\pi\bar{t}$ time translation. These are similar to the eigenstates of a time-independent Hamiltonian, which are invariant under any time translation. In our system, the tunneling states are even and odd superpositions of states localized on the islands \mathcal{I}_+ and \mathcal{I}_- . These are expected to be eigenstates of the system's Floquet operator F_m . As noted in the Introduction, $|\psi_{\text{even}}\rangle$ and $|\psi_{\text{odd}}\rangle$ are analogous to the ground state and first excited state of a double-well system, respectively. Because the Floquet operator is unitary, it has eigenvalues of the form

$$f = \exp(-2\pi i E / \hbar_{\text{eff}}), \quad (6)$$

where E is the corresponding eigenstate's *quasienergy*—the generalization of the notion of energy to time-periodic systems.

D. Numerical solution of the Floquet spectrum

To study dynamical tunneling in this system, we must numerically determine the Floquet spectrum and identify the even and odd Floquet states that are localized on the period-one fixed points of the Poincaré section. These will be dependent on the potential strength κ , modulation amplitude ϵ , and effective Planck's constant \hbar_{eff} . As the trapping potential is symmetric, the even and odd Floquet states are uncoupled. Our numerical procedure is to choose a regular grid in position space and then separately evolve a basis of even and odd combinations of position eigenfunctions for one period of the modulation. This determines the Floquet matrix F_m for the Hamiltonian H_m , which we diagonalize to find the Floquet states. The tunneling states are identified as being the even (odd) Floquet states having the largest overlaps with an even (odd) superposition of coherent states centered on the period-one fixed points of the classical phase space. We therefore can expect a localized state on one island to be formed by $|\phi_+\rangle = (|\psi_{\text{even}}\rangle + |\psi_{\text{odd}}\rangle)/\sqrt{2}$, and this will tunnel to a state $|\phi_-\rangle = (|\psi_{\text{even}}\rangle - |\psi_{\text{odd}}\rangle)/\sqrt{2}$ localized on the opposite island. The corresponding tunneling period is given by $T_{\text{tunnel}} = 2\pi\hbar_{\text{eff}}/\Delta E$, where ΔE is the quasienergy splitting of the tunneling states: $\Delta E = |E_{\text{even}} - E_{\text{odd}}|$.

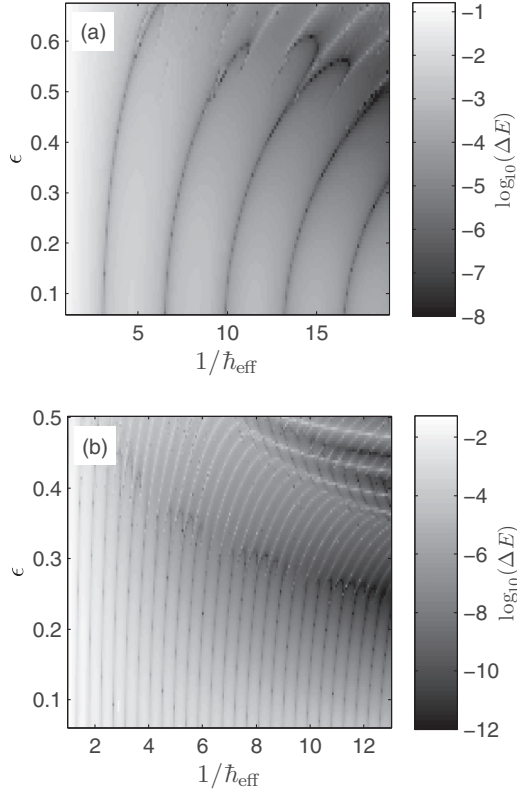


FIG. 3. Quasienergy splitting ΔE of the tunneling Floquet states as a function of the inverse effective Planck's constant $1/\hbar_{\text{eff}}$ and the modulation strength ϵ for the atom-chip Hamiltonian Eq. (2) for two different potential strengths. (a) $\kappa = 1.2$; (b) $\kappa = 2.0$.

III. RESULTS

In this section we investigate the dependence of the quasienergy splitting ΔE on the tunable parameters for our system κ , ϵ , and \hbar_{eff} . Typical results are shown in Fig. 3 for (a) $\kappa = 1.2$ and (b) $\kappa = 2.0$. These figures have several noteworthy features, many of which have been observed previously in other systems [17,18,22,31,32].

A. Overview

For our analysis, we divide the parameter space shown in Fig. 3 into two regions according to the characteristic behavior of the quasienergy splitting. First, we see in the bottom-left corner of Figs. 3(a)–3(b) that for a large parameter range the behavior of ΔE is not completely unruly, but instead some grooves and plateau structures are obvious. The dependence of ΔE on $1/\hbar_{\text{eff}}$ differs from the exponential behavior characteristic of Hamiltonians of the form $H = p^2/2 + V(q)$, while still being quite smooth. In this regime, which we call quantum regular regime (QRR), the quasienergy splitting periodically falls to zero. To the best of our knowledge, this has not been commented on in detail in previous studies—we account for the origin of these grooved structures in Sec. III B. This result constitutes the most significant theoretical development of this paper.

Second, in the top-right corners of Figs. 3(a)–3(b), classical chaos has the strongest influence on the system. This regime is characterized by the dramatic and apparently disorderly

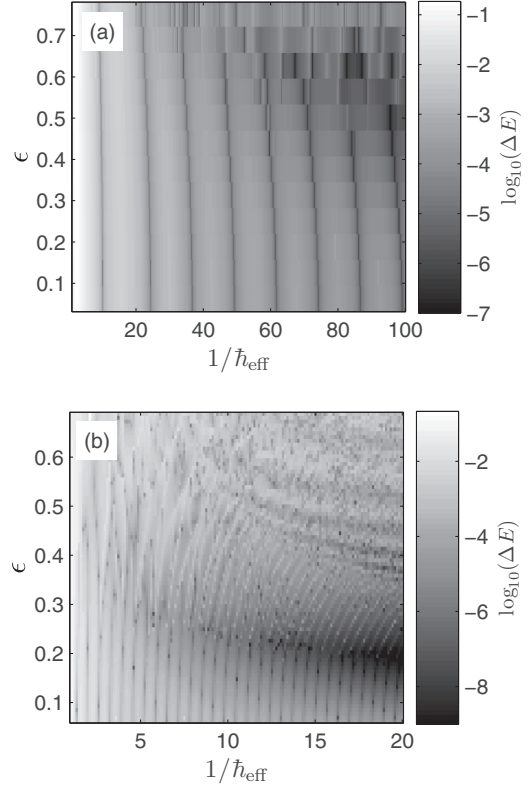


FIG. 4. Quasienergy splitting ΔE of the tunneling Floquet states as a function of the inverse effective Planck's constant $1/\hbar_{\text{eff}}$ and the modulation strength ϵ for the (a) quartic oscillator with Hamiltonian given by Eq. (7) and $\kappa = 2$; (b) nonlinear pendulum with Hamiltonian given by Eq. (8) and $\kappa = 1.5$.

fluctuations of ΔE [17,18,23], and we refer to it as the classical chaotic regime (CCR). In our discussion of the CCR, Sec. III C, we apply existing theories by Podolskiy and Narimanov [24] and Eltschka and Schlagheck [21] to our specific scenario. Comparison of these theories with our numerical simulations shows good agreement and completes our analysis of the present atom-chip system in the single-particle regime.

We note that the division described above is not peculiar to the atom-chip Hamiltonian but appears to be a general feature of driven quasi-integrable systems. We have also diagonalized the Floquet operator for other nonlinear potentials such as the quartic oscillator,

$$H = \frac{p^2}{2} + \kappa(1 + \epsilon \cos t)q^4, \quad (7)$$

as well as the nonlinear pendulum,

$$H = \frac{p^2}{2} - \kappa(1 + \epsilon \cos t) \cos q, \quad (8)$$

and found the same features. Sample results are shown in Fig. 4. The latter Hamiltonian has been studied elsewhere both theoretically [17,18,30,31] and experimentally [9,12].

B. Quantum regular regime

We define the quantum regular regime as the region in parameter space where the quasienergy splitting ΔE varies smoothly, apart from the apparently periodic troughs where

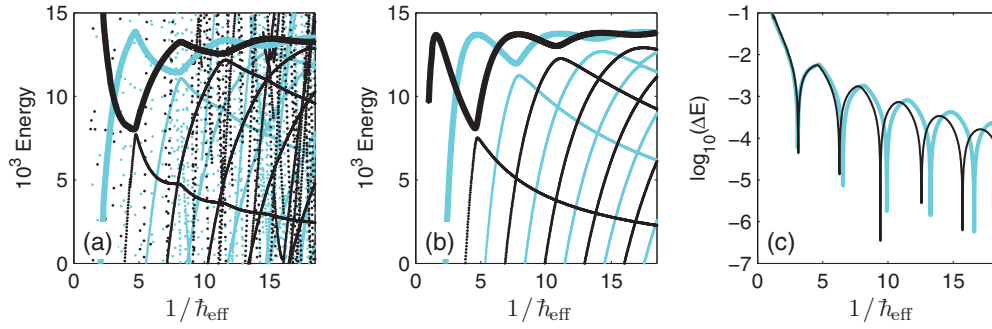


FIG. 5. (Color online) Comparison of the Floquet spectrum of the full Hamiltonian H_m , Eq. (2), and the energy spectrum of the integrable approximation H_i , Eq. (9), for $\kappa = 1.2$ and $\epsilon = 0.1$. (a) The quasienergy spectrum of the full Hamiltonian as a function of $1/\hbar_{\text{eff}}$. The black points are for the even Floquet states, and the cyan (gray) points are for the odd Floquet states. The points corresponding to the tunneling states are joined with thick solid lines of the same color. (b) The energy spectrum of the integrable approximation as a function of $1/\hbar_{\text{eff}}$, with the same color scheme as for (a). The structures here are very similar to those in (a), indicating that the integrable approximation captures the important features of the full Hamiltonian in this regime. (c) A plot of the quasienergy difference of the even and odd tunneling states as a function of $1/\hbar_{\text{eff}}$. Black curve: full Hamiltonian. Cyan (gray) curve: integrable approximation.

the splitting goes to zero. In both Figs. 3(a) and 3(b) it is the region for which $\epsilon \lesssim 0.3$. The origin of this behavior can be seen by plotting the quasienergy spectrum of the Floquet operator F_m as in Figs. 5(a)–5(b). We find that at regularly spaced values of $1/\hbar_{\text{eff}}$, a Floquet state not involved in the tunneling deflects the tunneling state of the same parity through an avoided crossing scheme very similar to the result of a typical first-order perturbation theory calculation.

This scenario has previously been invoked in the context of tunneling or dynamical tunneling suppression [31,32], often in order to describe the phenomena inducing the CCR fluctuations [17,18,33]. More generally, it has been noted that level repulsion occurs for dynamical tunneling in the presence of a chaotic sea [21,23,24]. However, we demonstrate here that this effect has no chaotic origin. This conclusion was also reached in Ref. [33] by different means. Here we make use of secular perturbation theory [2] and assume that $\kappa - 1$ is of order ϵ and, therefore, within the islands of regular motion we have both $q = \mathcal{O}(\sqrt{\epsilon})$ and $p = \mathcal{O}(\sqrt{\epsilon})$. This allows us to derive a second-order integrable approximation H_i to the full atom-chip Hamiltonian H_m given by Eq. (2) as [2]

$$H_i = \frac{3}{1024} (p^2 + q^2)^3 + \frac{3(\kappa - 2)}{64} (p^2 + q^2)^2 + \frac{6(\kappa - 1) - 3(\kappa - 1)^2 + \epsilon^2}{24} p^2 + \frac{6(\kappa - 1) - 3(\kappa - 1)^2 - 5\epsilon^2}{24} q^2. \quad (9)$$

We find that this integrable approximation represents the classical dynamics of H_m reasonably well up to $\kappa = 1.3$ and $\epsilon = 0.6$. This can be seen by comparing the Poincaré sections for the full Hamiltonian Eq. (2) and the integrable approximation Eq. (9) in Fig. 6. Also, the prediction of the distance between the period-one fixed points of the integrable approximation Eq. (9) and the full Hamiltonian Eq. (2) is shown in Fig. 2 as a function of κ for three values of ϵ .

To proceed we quantize the integrable Hamiltonian H_i , Eq. (9). In principle, we could choose any operator ordering; given the symmetry of Eq. (9) we choose symmetric ordering.

This is then easily diagonalized numerically, and the resulting spectrum is plotted in Fig. 5(b). This should be compared to the spectrum of the Floquet operator F_m for the full Hamiltonian shown in Fig. 5(a). Qualitatively the spectra are similar and

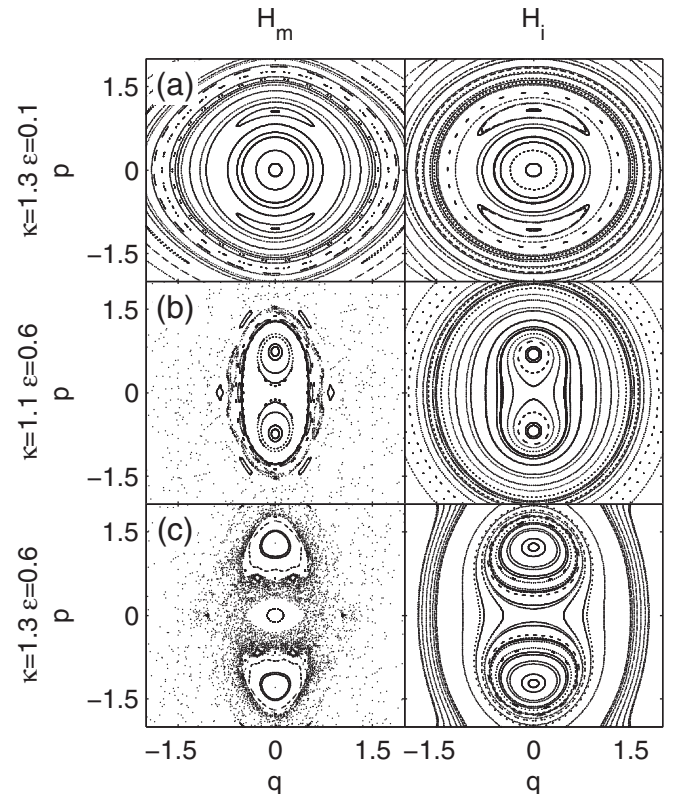


FIG. 6. Comparison of the Poincaré sections for the full Hamiltonian H_m , Eq. (2), and the integrable approximation H_i , Eq. (9) at $t = 0$, for (a) $\kappa = 1.3$ and $\epsilon = 0.1$, (b) $\kappa = 1.1$ and $\epsilon = 0.6$, (c) $\kappa = 1.3$ and $\epsilon = 0.6$. Although the presence of chaos for H_m in this latter regime makes the Poincaré sections of H_m and H_i look rather different, we find good agreement for the regular regions. The quantum behavior of the two systems agree for relatively large values of \hbar_{eff} as shown in Sec. III B.

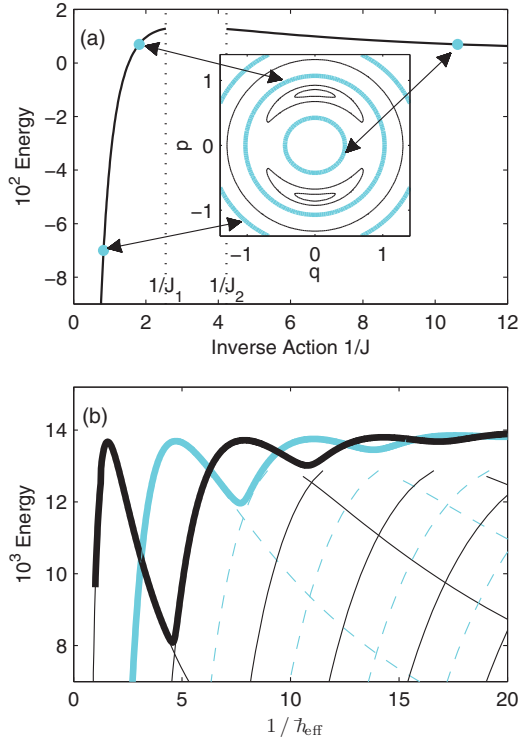


FIG. 7. (Color online) (a) Energy versus inverse action for the trajectories of the integrable approximation H_i that are not located on the islands (solid black curve). The gap occurs due to the presence of the islands. The inset shows selected trajectories of H_i . The energy of the trajectories in cyan (gray) are denoted in the main figure by cyan (gray) points as indicated by the arrows. (b) Energy of the semiclassical and quantum states as a function of $1/\hbar_{\text{eff}}$. The thin curves are the EBK quantization of the trajectories of H_i , Eq. (9). The thin solid black curves correspond to even parity states, and the thin dashed cyan (gray) curves to odd parity states. The thick black curve is the energy of the even tunneling state, and the thick cyan (gray) curve is the energy of the odd tunneling state, both found via the numerical diagonalization of H_i , Eq. (9). The avoided crossings of the quantum tunneling states with other states of the same parity are clearly visible.

quantitatively the prediction for the quasienergy splittings of the tunneling states are in good agreement with that found from the full Hamiltonian as shown in Fig. 5(c). We conclude that the tunneling states of the integrable approximation contain the essential features of the full system for $\kappa \lesssim 1.3$, $\epsilon \lesssim 0.6$, and $1/\hbar_{\text{eff}} \gtrsim 1$. It was previously shown that the enhancement of tunneling does not require chaos but can originate from avoided crossings in the Floquet spectrum [33]. Here we have demonstrated that even nonintegrability is not necessary.

To understand the quasiperiodic vanishing of the difference in quasienergy of the tunneling Floquet states as a function of \hbar_{eff} , we first plot in Fig. 7(a) the energy of the classical trajectories of H_i not located on the islands for $\kappa = 1.2$ and $\epsilon = 0.1$ in Fig. 7(a) as a function of the inverse action J^{-1} , where [2]

$$J = \frac{1}{2\pi} \oint p dq. \quad (10)$$

A gap exists in the curve for the range of the inverse action $2.5 \lesssim J^{-1} \lesssim 4.2$ corresponding to energies $E \gtrsim 1.29 \times 10^{-2}$

for which the classical trajectories are instead located on the islands.

We can now apply the Einstein-Brillouin-Keller (EBK) quantization method, which states that in order to correspond to a quantum eigenstate, the trajectories must satisfy

$$J = \hbar_{\text{eff}}(n + 1/2) \quad \text{with } n \in \mathbb{N}. \quad (11)$$

This will discretize the curve of energy versus inverse action in Fig. 7(a) for any particular value of \hbar_{eff} . Now as $1/\hbar_{\text{eff}}$ is increased, the spacing of the points along the x axis will also be increased, and particular eigenstates will move from the left-hand part of the curve (outside of the islands) to the right-hand part (inside the islands) and have a strong effect on the tunneling states. The energy of EBK quantized trajectories for $n = 0$ to $n = 10$ is plotted in Fig. 7(b)—even trajectories as thin black solid curves and odd trajectories as thin cyan (gray) dashed curves. The thick solid black curve is the energy of the even tunneling state, and the thick solid cyan (gray) curve is the energy of the odd tunneling state, both found from numerical diagonalization of the integrable approximation to the full Hamiltonian, Eq. (9). In Fig. 5 it is easy to see the avoided level crossings between Floquet states with the same parity. The curve for the quasienergy of each tunneling Floquet state changes direction at each avoided crossing, resulting in regular crossings of the quasienergies of the odd and even Floquet tunneling states, resulting in $\Delta E = 0$ and an infinite tunneling period. It seems quite reasonable that this explanation applies directly to the quasi-integrable Hamiltonian (2) in the QRR regime.

We have found that the spacing of the occurrences of $\Delta E = 0$ as a function of $1/\hbar_{\text{eff}}$ decreases with increasing κ . For example, it can be seen in Fig. 3 that the spacing of the valleys as a function of $1/\hbar_{\text{eff}}$ decreases between (a) with $\kappa = 1.2$ and (b) with $\kappa = 2.0$. This can be explained in the following manner. We find that the period-one islands remain of a similar phase space area for a given κ . Let the *minimum* action of any closed trajectory that lies entirely *outside* the islands be denoted as J_1 . Likewise, let the *maximum* action of any closed trajectory that lies entirely *inside* the islands be denoted as J_2 . The n th (with n large enough) crossing then will occur between $1/\hbar_{\text{eff}} = (n + 3/2)/J_1$ and $(n + 1/2)/J_2$. As κ increases, the distance between the islands in phase space increases, meaning J_1 and J_2 increase, and the spacing between the n th and $(n + 1)$ th quasi-energy degeneracy of the tunneling states will decrease. This is in agreement with the behavior of the Floquet spectrum of the full system.

In summary, in this section we have shown that the quantized integrable approximation Eq. (9) accounts for *all* the significant features of dynamical tunneling of the full system Hamiltonian Eq. (2) in the QRR. Therefore, we have demonstrated that the underlying classical nonintegrability of the full system has little effect in the QRR.

C. Classical chaotic regime

The defining characteristic of the classical chaotic regime is the irregular and large fluctuations of the quasienergy splitting ΔE as the parameters $1/\hbar_{\text{eff}}$ and ϵ are varied. Before considering the fluctuations, we comment on the coarse behavior of the tunnel splitting as we enter the CCR

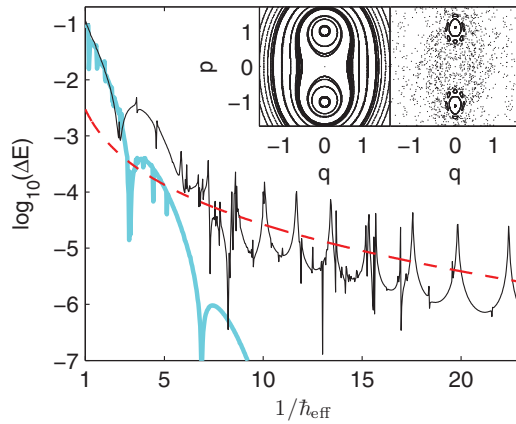


FIG. 8. (Color online) Quasienergy splitting of the tunneling Floquet states versus $1/\hbar_{\text{eff}}$ for $\kappa = 1.2$, $\epsilon = 0.75$. Thin solid black line: Exact result. Thick cyan (gray) solid line: Numerical diagonalization of the integrable approximation. Dashed red line: Result of the Podolskiy-Narimanov theory with the proportionality coefficient of Eq. (12) as a fitting parameter. Inset: Poincaré sections of the full Hamiltonian (right) and of its integrable approximation (left). The tunneling behavior of the full Hamiltonian H_m [Eq. (2)] agrees with the integrable approximation H_i [Eq. (9)] as long as the quantum coarse-graining effect prevents the quantum particle from seeing the layers of chaos. For smaller values of \hbar_{eff} , tunneling is enhanced by the presence of chaos in the underlying classical phase space according to the Podolskiy-Narimanov model [24].

from the QRR, by choosing ϵ near the upper boundaries of Figs. 3(a)–3(b) and then increasing $1/\hbar_{\text{eff}}$.

Averaging over the fluctuations of the quasienergy difference of the Floquet states as a function of $1/\hbar_{\text{eff}}$, we find that the overall tendency of the tunneling splitting variation resembles an exponential decrease with increasing $1/\hbar_{\text{eff}}$, as expected for dynamical tunneling phenomena [22,34]. It is not surprising that the tunnel splitting tends to decrease as the potential strength κ is increased and the two islands move away from each other in phase space. However, it should be noted that after initially decreasing with increasing ϵ , ΔE starts increasing again as the system enters the CCR [17]. This latter phenomenon can be attributed to so-called chaos-assisted tunneling. This occurs when the dominant transport mechanism from one island to the other is no longer direct quantum transport as in a regular system but instead a three-step process. First, particles tunnel from the center of one island to the sea of chaos, then are *classically* transported through the chaotic sea from the vicinity of this island to the vicinity of the other, and then eventually tunnel from the sea of chaos to the center of this latter island [24]. The complete behavior of ΔE as $1/\hbar_{\text{eff}}$ is increased is shown in Figs. 8 and 9. A number of regions with distinct changes in the average slope of the $\log_{10}(\Delta E)$ versus $1/\hbar_{\text{eff}}$ curve are evident. These indeed can be partially accounted for by changes of the dominant transport mechanism from one island to the other.

For large values of \hbar_{eff} , we expect the quantum behavior of chaotic systems to approach that of regular systems, as the quantum “coarse-graining” makes them insensitive to the presence of fine phase-space structures. We are, hence, in the QRR, where the quasienergy splittings of the time-modulated system agree with those of the integrable approximation,

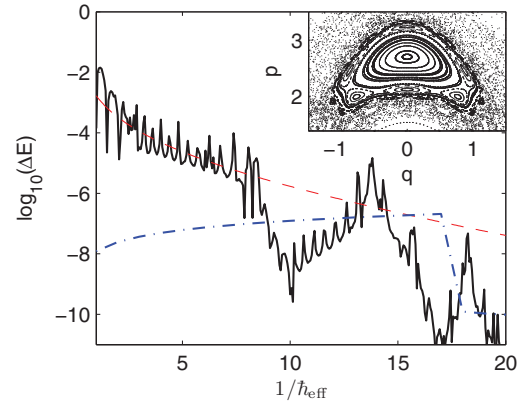


FIG. 9. (Color online) Quasienergy splitting of the tunneling Floquet states as a function of \hbar_{eff} for $\kappa = 2$, $\epsilon = 15/32$. Solid black line: Exact numerical result. Red dashed line: Podolskiy-Narimanov theory (one fitting parameter). Blue dash-dot line: Eltschka-Schlagheck theory (no fitting parameter). Inset: Poincaré section centered on \mathcal{I}_+ . One secondary resonance chain is clearly dominant. For large values of \hbar_{eff} , the quantum coarse-graining prevents the system from seeing these small phase-space structures, and its behavior is then well described by Eq. (12). For smaller values of \hbar_{eff} the Eltschka-Schlagheck model [21], which takes the island chain into account, shows much better agreement with the numerical data.

showing that the dominant transport mechanism from one island to the other is direct tunneling.

Starting from the QRR and decreasing the effective Planck’s constant, we reach a regime where \hbar_{eff} is comparable to the phase-space area of the period-one islands of regular motion. If chaos is present in the classical phase space, the dominant tunneling mechanism is then expected to be chaos-assisted tunneling, as described earlier. According to Podolskiy and Narimanov [24], the tunnel splittings yielded by such a mechanism have the following dependence on \hbar_{eff} :

$$\Delta E \propto \hbar_{\text{eff}} \frac{\Gamma(A/\pi\hbar_{\text{eff}}, 2A/\pi\hbar_{\text{eff}})}{\Gamma(A/\pi\hbar_{\text{eff}} + 1, 0)}, \quad (12)$$

where A is the phase-space area of one island of regular motion and Γ the upper incomplete Γ function [35]. We observe the transition from the QRR to this regime in Fig. 8, where the tunneling behaviour of H_m diverges from the approximate exponential behaviour yielded by H_i as \hbar_{eff} is decreased. A more generic result than Eq. (12) for the chaos-assisted tunneling splitting has recently been found by Bäcker *et al.* [26].

However, neither the Podolskiy-Narimanov model nor the Bäcker *et al.* model takes into account the fine features of the classical phase space, for example, partial dynamical barriers embedded in the sea of chaos [36], or the internal structure of the islands of regular motion themselves. Therefore, even if some systems are well described by these models for a certain range of \hbar_{eff} , decreasing this parameter, and, therefore, the resolution of the quantum coarse-graining, can make the system “see” those small structures. As can be seen in Fig. 9, this leads to dramatic deviations from Eq. (12).

For $\hbar_{\text{eff}} \lesssim 0.1$, it is once again possible to explain the observed deviations by a change in the dominant transport

mechanism from one island to the other. It is known that in the semiclassical limit $\hbar_{\text{eff}} \rightarrow 0$, tunneling through regular phase space is greatly facilitated by the presence of resonance chains [19,20]. It is therefore expected that for low \hbar_{eff} tunneling between an island of regular motion and the sea of chaos will be enhanced by the presence of a secondary resonance chain embedded in this island.

A model reflecting this idea has been developed by Eltschka and Schlagheck [21], with a detailed description given in Ref. [25]. Let us assume each of the symmetric islands of regular motion supports a $r:s$ secondary resonance chain—i.e., where s internal oscillation periods match r driving periods, and r subislands are visible on the Poincaré section. This situation is well illustrated in our system for the parameters presented in Fig. 9 (see inset). First, the authors approximate the dynamics within the island to that of a pendulum and treat the pendulum potential $2V_{r,s} \cos r\theta$ as a perturbation. This perturbation couples the ground state $|\psi_0\rangle$ of the unperturbed approximate Hamiltonian only to the excited states $|\psi_{lr}\rangle$ where l is an integer. In the following, we will denote $|\phi_l\rangle = |\psi_{lr}\rangle$. Denoting by $2\pi I_c$ the phase-space area of the island of regular motion (measured on a Poincaré section), they calculate the coupling of the unperturbed ground state of the island to its k th ϕ -type state through this resonance, where k is defined by $I_{(k-1)} < I_c < I_k$ (I_l , $l \in \mathbb{N}$ denotes the action associated with the l th ϕ state). In other words, they calculate the coupling of the approximate ground state of the island to the lowest ϕ -state localized in a region where chaos is present for the exact Hamiltonian. They then assume that this coupling describes the effective coupling of ϕ_0 to the sea of chaos and model the latter by two matrices of the Gaussian orthogonal ensemble (one for each parity), which means that they neglect the effects of partial barriers in the chaotic part of phase space. Using the results from Ref. [23], they are therefore able to calculate an expectation value for the logarithm of the quasienergy splittings for each set of parameters, which we compare to our numerical results in Fig. 9.

We find reasonable qualitative and quantitative agreement in the range $\hbar_{\text{eff}} < 0.1$, which is expected as this is precisely the order of magnitude of the phase-space area of the dominant chain's resonances. We also observe an effect already noted by Eltschka and Schlagheck [21], namely the fact that the sharp decrease of the analytically calculated tunneling splittings is shifted to lower values of \hbar_{eff} as compared to the similar decrease of the splittings obtained from the numerical simulations. Such steps occur when the value of the index k changes, i.e., every time an unperturbed ϕ state of the approximate Hamiltonian crosses the somewhat artificial limit I_c of the island of regular motion. This happens for every integer l such that $I_c = \hbar_{\text{eff}}(lr + 1/2)$ (in our case, $r = 6$ and $l = 1$). It is known, however, that states that are neither chaotic nor regular (*hierarchical* states: see Ref. [37]) can be localized in the vicinity of the island. Therefore, the “effective value” of the islands' phase-space area could be a little higher than $2\pi \times I_c$. This could account for the observed shift of the step.

Recently, a unified description that can predict tunnel splittings from the direct tunneling regime to the resonance assisted regime has been developed [38]. It is hopeful that this theory would provide an improved description of the data

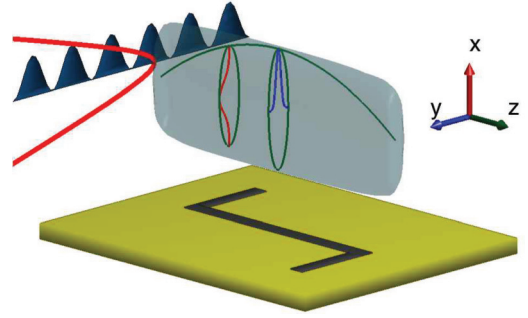


FIG. 10. (Color online) Schematic of the arrangement of condensate, confining potentials, and atom-chip surface (yellow) with characteristic z -shaped wire. The atom-chip potential has the form Eq. (2) along $x = q$ (red) and is weakly harmonic along z (potential not shown). Superimposed is an optical lattice potential (blue), freezing out the dynamics along y . The gray shaded volume is the resulting isodensity surface of a trapped BEC. Embedded density profiles along the x , y , z , coordinate directions are also sketched.

in Fig. 9; however, its complexity puts it beyond the scope of this paper.

IV. PROSPECTS FOR EXPERIMENTS

We now examine the feasibility of performing dynamical tunneling experiments that explore the effects presented in the previous sections with a Bose-Einstein condensate in a magnetic microtrap. To this end we discuss the realization of a one-dimensional Hamiltonian in Sec. IV A, realistic parameters for the trapping potential in Sec. IV B, the effects of atomic interactions in Sec. IV C, the initial state creation and loading in Sec. IV D, and, finally, condensate sizes and inelastic losses in Sec. IV E.

A. Confinement geometry

A key difficulty is that the form of the Hamiltonian Eq. (2) is realized in terms of the two-dimensional (2D) radial coordinate $r = \sqrt{x^2 + y^2}$ of the atom-chip trap, see Appendix A. Instead, we require it to describe a 1D degree of freedom, say $q = x$. Without this constraint, the islands of classically bounded regular motion can be dynamically linked via the second radial dimension (y). Classical diffusion can then populate the other island and mask the signature of dynamical tunneling. While the tunneling and diffusion rates will, in general, differ markedly, it would be desirable to avoid this effect altogether by freezing out the dynamics in the y direction. This could be achieved by applying an optical lattice formed by two laser beams propagating along the $\pm y$ directions and confining the atoms in one well of the lattice, as sketched in Fig. 10.

In contrast to the y dimension, the z dimension can be very weakly confined on an atom chip. The condensate in that direction then has an approximately “infinite” extension. We will check this assumption below in Sec. IV E.

B. Accessible tunneling parameters

We begin by proposing a regime in which it is feasible to observe dynamical tunneling. From a practical point of view, we wish to minimise the tunneling period and the sensitivity

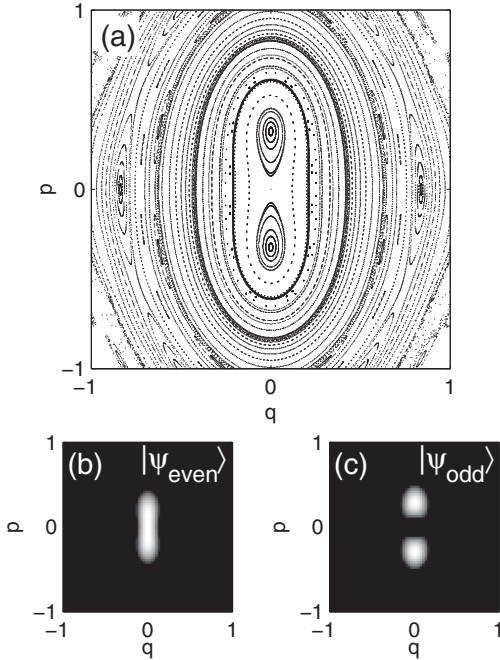


FIG. 11. (a) Poincaré section at $t = 0$ for the proposed experimental parameters $\kappa = 1.01$, $\hbar_{\text{eff}} = 1/73$, $\epsilon = 0.48$. Note that no chaos is present between the islands. (b) Husimi function for the even tunneling state. (c) Husimi function for the odd tunneling state.

of the tunneling to any small fluctuations in experimental parameters. Distinguishable period-one islands appear in the Poincaré section for $\kappa > 1$, and the closer the islands are in phase space, the shorter the tunneling period. However, if the two islands are too close to each other, separating them in time-of-flight absorption images could be challenging. High values of \hbar_{eff} yield faster tunneling but require very tight trapping potentials. A convenient and accessible choice of parameters within the QRR is $\kappa = 1.01$, $\hbar_{\text{eff}} = 1/73$, and $\epsilon = 0.48$, which gives a relatively short tunneling period of 159 modulations of the trapping potential. This has the additional advantage that the tunneling period is relatively insensitive to small, uncontrolled experimental variations in the exact value of the parameters, with the strongest dependence being on κ . We calculate that the following variations would induce shifts of less than 10% in the tunneling period:

$$1.009 < \kappa < 1.011, 1/77 < \hbar_{\text{eff}} < 1/69, 0.37 < \epsilon < 0.59. \quad (13)$$

The Poincaré section and Husimi functions of the two tunneling Floquet states are shown in Fig. 11. To achieve this with a BEC of ^{87}Rb atoms in the $F = 2$, $m_F = 2$ magnetic substate confined on an atom chip would require a current through the trapping wire of $I = 63$ mA and a bias magnetic field of $B_b = 5$ G. In the limit of an infinitesimal wire, this yields a trap $25 \mu\text{m}$ from the wire which, when combined with an axial magnetic field of $B_0 = 0.25$ G, has a radial trapping frequency in the harmonic approximation of $\omega_r = 2\pi \times 5$ kHz. At such distances wire imperfections that could distort the confining potential and cause cloud fragmentation can be avoided [39]. The trap depth is of the

same order of magnitude as the atomic Zeeman energy from the magnetic field due to the wire current at the location of the trap minimum. For our parameters it is roughly equal to $E_{\text{mag}} = gm_F\mu_B B_b \approx 0.3$ mK, more than sufficient to trap a BEC at nanokelvin temperatures.

C. Bose-Einstein condensates and mean-field effects

So far we have considered the physics of single atoms within the driven potential. This has previously been sufficient to describe experiments in very dilute thermal or condensed gases [9,12]. However, to work with a trapping potential with a single minimum, to controllably load small regions of phase space, and to still be able to image the resulting dynamics, it is necessary to use atoms that are sufficiently cold and dense that they are Bose condensed. In realistic BECs nonlinear mean-field interactions arising from atomic s -wave collisions can play an important role in the dynamics [40]. These can be described using the one-dimensional Gross-Pitaevskii equation (GPE),

$$i\hbar_{\text{eff}} \frac{\partial}{\partial t} \psi = \left[-\frac{\hbar_{\text{eff}}^2}{2} \frac{\partial^2}{\partial q^2} + V(q,t) + U_{1D} |\psi|^2 \right] \psi. \quad (14)$$

Here the condensate wave function $\psi(q,t)$ is normalized to 1 and the potential is $V(q,t) = \kappa(1 + \epsilon \cos(t))(1 + q^2)^{1/2}$. The relation between the effective one-dimensional interaction-strength U_{1D} and the physical parameters of the system is derived in Appendix B.

We have performed numerical simulations of the 1D Gross-Pitaevskii equation (14) with the BEC initially loaded in the pure Floquet superposition state $|\phi_+\rangle$. For the case described in Sec. IV B, we find that dynamical tunneling oscillations can be observed with Eq. (14) for nonlinearities up to about $U_{\text{max}} = 1.8 \times 10^{-4}$, beyond which the nonlinearity shuts down dynamical tunneling. For these particular parameters we have found that this is an example of macroscopic quantum self-trapping, which we have analyzed in detail elsewhere [41]. For the purposes of this paper, we choose $U_{1D} = 1 \times 10^{-4}$ which results in unhindered dynamical tunneling oscillations as demonstrated in Fig. 12(b), where we show the momentum-space distribution at integer multiples of the modulation period. This momentum-space image constitutes a direct experimental observable, as standard time-of-flight expansion and absorption imaging techniques convert the center-of-mass momentum into spatial positions that are easily resolved [42]. An improved signal-to-noise ratio can potentially be obtained by imaging along the weakly trapped z direction, as the atomic density will be spread across fewer pixels on the camera.

Finally, we note that the onset of suppression of dynamical tunneling by nonlinearities depends strongly on the system parameters, and in some regimes does not occur at all. We have studied the presence and absence of macroscopic quantum self-trapping in Ref. [41].

D. Experimental and numerical initial states

In this section we consider how to best load the initial Floquet superposition $|\phi_+\rangle$ experimentally, as well as the effects of imperfect loading. In Fig. 12(c) we show the results of a simulation with the same parameters as for Fig. 12(b), but

with the initial state being a BEC dynamically prepared from the ground state of the trapping potential such that it obtains a large overlap with the Floquet superposition $|\phi_+\rangle$. We label the resulting state $|\varphi_+\rangle$. Numerically, we create $|\varphi_+\rangle$ as follows: (i) We assume an initial potential strength κ_{ini} , differing from κ . In the potential $V(q) = \kappa_{\text{ini}}(1 + \epsilon)(1 + q^2)^{1/2}$, we determine the condensate ground state using imaginary time evolution [42]. (ii) The resulting wave function $f_1(q)$ is given a momentum kick $f_2 = f_1 \exp[i p_0 \hbar_{\text{eff}} t]$. (iii) We vary κ_{ini} and p_0 to maximize the overlap $\langle \phi_+ | f_2 \rangle$ and finally take this as the initial state $|\varphi_+\rangle[\kappa_{\text{ini}}, p_0]$ for our simulation. We see the dynamical tunneling arising from this procedure in Fig. 12(c), where we have used $p_0 = 0.244$ and $\kappa_{\text{ini}} = 4.5$.

The corresponding experimental sequence is as follows: we begin with a stationary BEC trapped in the ground state of the magnetic potential with trap strength given by κ_{ini} . The wire current would then be slowly decreased by an amount $\delta I = 0.78$ mA and then suddenly switched back to 63 mA to start the cloud oscillating about the center of the trap minimum, acquiring the maximal momentum p_0 . When the BEC passes the bottom of the trap for the first time ($t = 0$), the simultaneous modulation of wire current and bias magnetic fields at $\epsilon = 0.48$ and $\Omega = 2\pi \times 4.975$ kHz begins, resulting in the loading of an equal superposition of the odd and even tunneling Floquet states with a fidelity of up to 95%. At this moment the trap strength is also changed to κ . Following the described sequence, the state $|\varphi_+\rangle$ can be directly created in the experiment.

On closer inspection, the simulations beginning with this initial state show a slightly different dynamical tunneling period compared to those that begin from a Floquet superposition. We find such modifications in the presence of nonlinear interactions whenever the initial state slightly differs from the exact Floquet state $|\phi_+\rangle$. As we vary κ_{ini} and p_0 used to define $|\varphi_+\rangle$, the tunneling period undergoes small but continuous changes. This effect is absent in the linear case with $U = 0$.

E. Condensate parameters

The parameters of Figs. 12(a)–12(c) amount to a condensate of $N = 171$ atoms [Eq. (B7)], assuming the axial extension of the condensate is $50 \mu\text{m}$, with a corresponding peak density of $2 \times 10^{14} \text{cm}^{-3}$. For comparison, we show in Figs. 12(d)–12(f) a second parameter set with much larger $\hbar_{\text{eff}} = 1/2$, with other parameters $\kappa = 1.3$, $\epsilon = 0.2$, and $U_{\text{1D}} = 0.01$, corresponding to $N = 20$ atoms. Realizing $\hbar_{\text{eff}} = 1/2$ would either require us to lower B_0 to 17 mG or increase ω_x to about $2\pi \times 300$ kHz. While challenging, precise imaging of small clouds of atoms as discussed here has been achieved [43,44]; however, the reliability of mean-field theory in this regime is questionable.

We estimate that three-body losses in this scenario would limit the BEC lifetime to a few hundred milliseconds [45] which is sufficiently long to conduct the experiment. The Majorana transition-induced losses will be negligible as $\omega_{\text{Larmor}}/\frac{d\theta}{dt} \gtrsim 10$ at all times, where θ is the angle between the magnetic field and the z axis at the position of a classical period-one resonance.

As mentioned in Sec. IV A, the freezing of the y direction could be achieved by applying an optical lattice formed by two

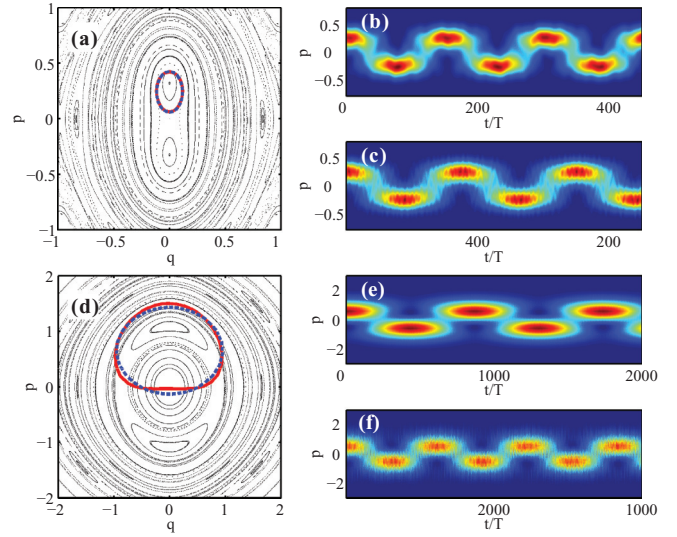


FIG. 12. (Color online) [(a)–(c)] Dynamical tunneling signatures from condensate mean-field theory according to Eq. (14) for parameters as in Fig. 11 and $U_{\text{1D}} = 1 \times 10^{-4}$. (a) Husimi function (full width at half-maximum) of the initial state located within the Poincaré section: (thick red, solid) initial Floquet state $|\phi_+\rangle$, (thick blue, dashed) experimentally accessible Gaussian approximation as explained in the text, $|\varphi_+\rangle$. (b) Dynamical tunneling in momentum space from initial Floquet state and (c) from initial Gaussian approximation as explained in the text. [(d)–(f)] The same as (a)–(c) but for parameters $\kappa = 1.3$, $\hbar_{\text{eff}} = 0.5$, $\epsilon = 0.2$, and $U_{\text{1D}} = 0.01$, with $p_0 = 0.65$ and $\kappa_{\text{ini}} = 0.4$.

laser beams propagating along the $\pm y$ directions and confining the atoms in one well of the lattice. The transverse (radial) size of the condensate with 171 atoms is less than 200 nm, which would easily fit into a single lattice site. Therefore, not only would dynamical tunneling take place exclusively in the plane perpendicular to the lattice, it would also occur in a single lattice site.

Finally, we have assessed the influence of the trapping potential in the z dimension and of experimental imperfections in the trap alignment. We have explicitly verified that the weakly confined z dimension can be ignored, as mentioned in Sec. IV A. To this end, we modelled the dynamics of Fig. 12 using the full two-dimensional GPE, Eq. (B3), with a weak harmonic trap in the z direction. The axial condensate wave function had a nontrivial Thomas-Fermi profile [42]. The tunneling signal in momentum space is as clear as those shown in Figs. 12(b) and 12(c), even accounting for imaging along the z axis. Furthermore, in two-dimensional simulations we have found the dynamical tunneling to be robust to changes in the initial state away from the ideal Floquet superposition, as well as small offsets from the trap center.

Unfortunately, it seems that the tight trapping potentials combined with the small atom numbers present a significant experimental challenge for dynamical tunneling with BECs to be realized as described here. The small atom numbers found for these examples are mostly due to the need to freeze-out dynamics in the y direction. An investigation to what extent dynamical tunneling can still be identified if dynamics in the y direction is retained would be of interest but is beyond the scope of the present paper. Note that the small number of atoms

is required in order to keep the peak-density low enough for the effect of interactions to remain small. The effect of stronger interactions can be quite complicated, but elsewhere we have found that it is possible to observe dynamical tunneling in regimes with much larger atom numbers [41].

V. CONCLUSIONS

We have studied dynamical tunneling in a driven 1D single-well potential provided by the magnetic field of a current-carrying wire on an atom chip. An experiment performed in this geometry would provide the possibility of studying the quantum-classical transition as a function of the effective Planck's constant. It also has a clear correspondence to the classical dynamical picture, uncomplicated by coherences between neighboring wells of a standing wave [12].

We have analyzed the dependence of the dynamical tunneling rate with the experimental parameters and observed that it fluctuates considerably, a feature previously observed for other trapping potentials. In the limiting case of the quantum regular regime, we were able to relate the variation in the tunneling rate to the energy spectrum of an integrable Hamiltonian. In the classical chaotic regime, the variation in the tunneling rate is linked to a chaos-assisted tunneling phenomenon for high \hbar_{eff} . For lower \hbar_{eff} we have underlined the role of classical resonances linking the islands of regular motion with the sea of chaos.

Finally, we have considered the experimental prospects for realizing dynamical tunneling with a BEC in a magnetic microtrap. We have found that dynamical tunneling would be observable on a 10-ms time scale for realistic atom-chip parameters provided the dynamics in the plane perpendicular to the motion could be frozen out. However, this requires BECs with a rather small number of atoms. Our conclusions hold in the presence of nonlinearities due to atomic interactions as long as these are not too large.

ACKNOWLEDGMENTS

This research was supported under the Australian Research Council's Discovery Projects funding scheme (Projects No. DP0343094 and No. DP0985142) and by the ARC Centre of Excellence for Quantum-Atom Optics (Project No. CE0348178). G.J.M. acknowledges the support of the Australian Research Council Grant No. FF0776191. M. L. thanks Dominique Delande, Christopher Eltschka, and Peter Schlagheck for stimulating discussions. We thank Tod Wright for a careful reading of the manuscript.

APPENDIX A: ATOM-CHIP HAMILTONIANS

We consider atoms trapped in a magnetic potential formed by a current flowing in the positive z direction along single infinite conductor, with a constant bias field B_b in the negative y direction. This forms a 2D potential in the x and y dimensions. For now we will ignore any dynamics in the z dimension—this is reasonable as on typical atom chips the trapping potential in this dimension is much weaker and the dynamics are correspondingly slower.

The magnetic field strength a distance $\sqrt{x^2 + y^2}$ from the conductor will be

$$|B(r)| = \frac{\mu_0}{2\pi} \frac{I}{\sqrt{x^2 + y^2}}. \quad (\text{A1})$$

The bias field B_b cancels the field from the wire along the line defined by

$$x = x_0 = \frac{\mu_0 I}{2\pi B_b}, \quad (\text{A2})$$

where the field gradient will be

$$|B'| = \frac{\mu_0}{2\pi} \frac{I}{x_0^2} = \frac{B_b}{x_0}. \quad (\text{A3})$$

We define $x' = x - x_0$ and $r = \sqrt{x'^2 + y^2}$. If we add a small, possibly time-dependent, offset field in the z dimension of magnitude B_0 , then the magnitude of the field at a distance r from the minimum can be approximated by

$$B = \sqrt{(rB')^2 + B_0^2}, \quad (\text{A4})$$

which will be valid for $r \ll x_0$ (for more detail see the next section). The radial potential that the atoms see will be

$$V(r) = gm_F \mu_B B_0 \sqrt{(B'/B_0)^2 r^2 + 1}, \quad (\text{A5})$$

where g is the Landé g factor, m_F is the magnetic sublevel that is trapped, and μ_B is the Bohr magneton. For $(B'/B_0)^2 r^2 \ll 1$ a Taylor expansion gives

$$V(r) = \frac{1}{2} gm_F \mu_B \frac{B'^2}{B_0} r^2 + \text{const.}, \quad (\text{A6})$$

i.e., the minimum of the potential is approximately harmonic with a radial trapping frequency of

$$\omega_r = B' \sqrt{\frac{gm_F \mu_B}{m B_0}}. \quad (\text{A7})$$

The system Hamiltonian is then

$$H = \frac{p^2}{2m} + gm_F \mu_B B_0 \sqrt{(B'/B_0)^2 r^2 + 1}. \quad (\text{A8})$$

We define the dimensionless quantities

$$\tilde{r} = \frac{B'}{B_0} r, \quad \tau = \Omega t, \quad \tilde{p} = \frac{B'}{B_0 m \Omega} p, \quad \tilde{H} = \frac{B'^2}{m \Omega^2 B_0^2} H, \quad (\text{A9})$$

where Ω will be the angular frequency of the modulation. After dropping tildes, we find our dimensionless Hamiltonian is

$$H = \frac{p^2}{2} + \kappa \sqrt{r^2 + 1}, \quad (\text{A10})$$

where we have defined the dimensionless parameter

$$\kappa = \frac{gm_F \mu_B B'^2}{m B_0 \Omega^2} \equiv \frac{\omega_r^2}{\Omega^2}. \quad (\text{A11})$$

The effective Planck's constant for this system is

$$\hbar_{\text{eff}} = \frac{\hbar B'^2}{B_0^2 m \Omega} \equiv \sqrt{\kappa} \frac{\hbar \omega_r}{gm_F \mu_B B_0}. \quad (\text{A12})$$

1. Modulation of the trapping potential

We now consider the possible ways we can modulate the trapping potential for the atoms. The magnetic field at location (x, y) is given by

$$\mathbf{B} = \left\{ -\frac{yB_w(t)}{\sqrt{x^2 + y^2}}, \frac{xB_w(t)}{\sqrt{x^2 + y^2}} - B_b(t), B_0(t) \right\}, \quad (\text{A13})$$

where $B_0(t)$ is the offset field along the z direction, $B_w(t)$ is the field from the 1D conductor, and $B_b(t)$ is the bias field along the y direction. We have

$$B_b(t) = B_{b0}(1 + f_b), \quad (\text{A14})$$

$$B_0(t) = B_0(1 + f_z), \quad (\text{A15})$$

$$\begin{aligned} B_w(t) &= \frac{\mu_0}{2\pi} \frac{I_0}{\sqrt{x^2 + y^2}} (1 + f_w), \\ &= \frac{x_0 B_{b0}}{\sqrt{x^2 + y^2}} (1 + f_w), \end{aligned} \quad (\text{A16})$$

where we have used the shorthand $f_a = f_a(t)$ for any modulation for $t > 0$. We also define the constant

$$x_0 = \frac{\mu_0 I_0}{2\pi B_{b0}}, \quad (\text{A17})$$

which is the location of the trap minimum with no driving.

The magnitude of the magnetic field can be shown to be

$$\begin{aligned} B^2 &= B_0^2(1 + f_z)^2 + \frac{B_{b0}^2}{(x_0 + x')^2 + y^2} [(1 + f_b)^2(x^2 + y^2) \\ &\quad + (f_b - f_w)^2 x_0^2 + 2(1 + f_b)(f_b - f_w)x'x_0]. \end{aligned} \quad (\text{A18})$$

where $x' = x - x_0$.

2. Choice of time-dependent modulations

Various Hamiltonians can be realized with appropriate choices of modulation of the magnetic fields and currents. Here we detail two that are potentially of interest.

1. $f_b = f_w = f_z$: In this case the trap minimum is stationary, and both the field gradient and the offset field B_0 are modulated. This yields the magnetic field

$$B = B_0(1 + f_b)(1 + \tilde{r}^2)^{1/2}, \quad (\text{A19})$$

which has a similar form to the modulated standing wave used in Refs. [9,12]—a potential with a stationary minimum but a modulated strength.

2. $f_b = 0, f_z = 0$: This case is probably the easiest experimentally, as only the current in the trapping wire needs to be modulated. This avoids any difficulties with inductances in the coils providing the bias and offset magnetic fields. The field in this case is

$$B = B_0 \left\{ 1 + \left(\frac{B'}{B_0} \right)^2 \left[y^2 + (x' - x_0 f_w)^2 \right] \right\}^{1/2}. \quad (\text{A20})$$

This potential has a constant strength but the position of its minimum oscillates.

In summary, the experimentally relevant Hamiltonians in dimensionless units are

$$H = \frac{p^2}{2} + \kappa(1 + \epsilon \cos \tau) [1 + (x'^2 + y^2)]^{1/2}, \quad (\text{A21})$$

$$H = \frac{p^2}{2} + \kappa \left[1 + y^2 + (x' - x_0 \epsilon \cos \tau)^2 \right]^{1/2}. \quad (\text{A22})$$

In this paper we have only considered Hamiltonian (A21) as this is analogous to the experiments performed in the modulated standing wave.

APPENDIX B: DIMENSIONAL REDUCTION OF THE GROSS-PITAEVSKII EQUATION

We begin with the standard Gross-Pitaevskii equation for the mean field of a condensate tightly confined along the y dimension [40]

$$\begin{aligned} i\hbar \frac{\partial}{\partial t} \psi(x, z) &= \left[-\frac{\hbar^2}{2m} \left(\frac{\partial^2}{\partial x^2} + \frac{\partial^2}{\partial z^2} \right) + V(x, z, t) \right. \\ &\quad \left. + \gamma_{2D} |\psi(x, z)|^2 \right] \psi(x, z), \end{aligned} \quad (\text{B1})$$

with

$$V(x, z, t) = V_0 [1 + \epsilon \cos(\Omega t)] \sqrt{1 + (x/d)^2}. \quad (\text{B2})$$

The effective 2D interaction is $\gamma_{2D} = 2\sqrt{2\pi}\hbar^2 a_s / (ma_y)$ [46], where a_s is the 3D scattering length and $a_y = \sqrt{\hbar / (m\omega_y)}$ the oscillator length in the frozen y direction. $\int dx dz |\psi|^2 = N$, the total 3D number of atoms. The parameters of the potential can be read from Eq. (A8) with the identification $x \leftrightarrow r$.

We now measure length in units of d and time in units of Ω^{-1} [see Eq. (3)] and employ the dimensionless wave function $\tilde{\psi} = \psi \sqrt{d/N}$, which is normalized to 1. Finally, relabelling $\tilde{\psi} \rightarrow \psi$, we obtain

$$\begin{aligned} i\hbar_{\text{eff}} \frac{\partial}{\partial t} \psi &= \left[-\frac{\hbar_{\text{eff}}^2}{2} \left(\frac{\partial^2}{\partial x^2} + \frac{\partial^2}{\partial z^2} \right) + V(x, z, t) \right. \\ &\quad \left. + U_{2D} |\psi(x, z)|^2 \right] \psi, \end{aligned} \quad (\text{B3})$$

where

$$V(x, z, t) = \kappa [1 + \epsilon \cos(t)] \sqrt{1 + x^2}. \quad (\text{B4})$$

Importantly $U_{2D} = N\gamma_{2D}/m\Omega^2 d^4$. We now eliminate the dimension z , assuming the size of the condensate in that direction, L_z , to be large and the dynamics hence slow. We simply set $\psi(x, z) = \tilde{\psi}(x)\phi(z)$, with $\phi(z) = \theta(\tilde{L}/2 - |z|)/\sqrt{\tilde{L}}$, where θ is the Heaviside function and $\tilde{L} = L_z/d$. Insertion into Eq. (B3) yields

$$i\hbar_{\text{eff}} \frac{\partial}{\partial t} \tilde{\psi} = \left[-\frac{\hbar_{\text{eff}}^2}{2} \frac{\partial^2}{\partial x^2} + V(x, t) + U_{1D} |\tilde{\psi}(x)|^2 \right] \tilde{\psi}, \quad (\text{B5})$$

with $U_{1D} = U_{2D}/L_z$. We obtain Eq. (14) by replacing $x \rightarrow q$ and have

$$U_{1D} = \frac{N\gamma_{2D}}{m\Omega^2 d^3 L_z} = \frac{2\sqrt{2\pi}\hbar^2 a_s N}{m^2 a_y \Omega^2 d^3 L_z} = \frac{2\sqrt{2\pi}\hbar^2 a_s N \kappa}{m a_y d L_z V_0}. \quad (\text{B6})$$

To rewrite Eq. (B6) in terms of the quantities $\hbar_{\text{eff}}, \kappa, \epsilon$, and U_{1D} that underly most of our numerical results, we substitute $d = B_0/B', V_0 = gm_F \mu_B B_0$ [comparing Eq. (B2) and Eq. (A8)]

and then use Eq. (A12) to arrive at

$$N = \frac{L_z U_{1D}}{2\sqrt{2\pi} a_s \hbar_{\text{eff}}^{3/2} \kappa^{1/4}} \sqrt{\frac{\omega_x}{\omega_y}}. \quad (\text{B7})$$

The atom numbers and densities quoted in Sec. IV C correspond to $L_z = 50 \mu\text{m}$, $\omega_z = 2\pi \times 18.6 \text{ Hz}$, $\omega_y = 2\pi \times 30 \text{ kHz}$ and other parameters as given in Sec. IV B.

-
- [1] C. Cohen-Tannoudji, B. Diu, and F. Laloë, *Quantum Mechanics* (Wiley-Interscience, New York, 2006).
- [2] A. J. Lichtenberg and M. A. Lieberman, *Regular and Chaotic Dynamics*, Vol. 38 of *Applied Mathematical Sciences*, 2nd ed. (Springer-Verlag, New York, 1992).
- [3] L. E. Reichl, *The Transition to Chaos* (Springer-Verlag, New York, 1992).
- [4] M. J. Davis and E. J. Heller, *J. Chem. Phys.* **75**, 246 (1981).
- [5] P. L. Gould, G. A. Ruff, and D. E. Pritchard, *Phys. Rev. Lett.* **56**, 827 (1986).
- [6] P. J. Martin, B. G. Oldaker, A. H. Miklich, and D. E. Pritchard, *Phys. Rev. Lett.* **60**, 515 (1988).
- [7] P. Szriftgiser, D. Guéry-Odelin, M. Arndt, and J. Dalibard, *Phys. Rev. Lett.* **77**, 4 (1996).
- [8] S. R. Wilkinson, C. F. Bharucha, K. W. Madison, Q. Niu, and M. G. Raizen, *Phys. Rev. Lett.* **76**, 4512 (1996).
- [9] D. A. Steck, W. H. Oskay, and M. G. Raizen, *Science* **293**, 274 (2001).
- [10] M. R. Andrews, C. G. Townsend, H.-J. Miesner, D. S. Durfee, D. M. Stamper-Kurn, and W. Ketterle, *Science* **275**, 637 (1997).
- [11] M. Albiez, R. Gati, J. F.ölling, S. Hunsmann, M. Cristiani, and M. K. Oberthaler, *Phys. Rev. Lett.* **95**, 010402 (2005).
- [12] W. K. Hensinger, H. Häffner, A. Browaeys, N. R. Heckenberg, K. Helmerson, C. McKenzie, G. J. Milburn, W. D. Phillips, S. L. Rolston, H. Rubinsztein-Dunlop *et al.*, *Nature* **412**, 52 (2001).
- [13] W. K. Hensinger, A. Mouchet, P. S. Julienne, D. Delande, N. R. Heckenberg, and H. Rubinsztein-Dunlop, *Phys. Rev. A* **70**, 013408 (2004).
- [14] S. Chaudhury, A. Smith, B. E. Anderson, S. Ghose, and P. S. Jessen, *Nature* **461**, 768 (2009).
- [15] D. A. Steck, *Nature* **461**, 736 (2009).
- [16] D. Ullmo, M. Grinberg, and S. Tomsovic, *Phys. Rev. E* **54**, 136 (1996).
- [17] A. Mouchet and D. Delande, *Phys. Rev. E* **67**, 046216 (2003).
- [18] A. Mouchet, C. Miniatura, R. Kaiser, B. Grémaud, and D. Delande, *Phys. Rev. E* **64**, 016221 (2001).
- [19] O. Brodier, P. Schlagheck, and D. Ullmo, *Phys. Rev. Lett.* **87**, 064101 (2001).
- [20] O. Brodier, P. Schlagheck, and D. Ullmo, *Ann. Phys.* **300**, 88 (2002).
- [21] C. Eltschka and P. Schlagheck, *Phys. Rev. Lett.* **94**, 014101 (2005).
- [22] S. Tomsovic and D. Ullmo, *Phys. Rev. E* **50**, 145 (1994).
- [23] F. Leyvraz and D. Ullmo, *J. Phys. A: Math. Gen.* **29**, 2529 (1996).
- [24] V. A. Podolskiy and E. E. Narimanov, *Phys. Rev. Lett.* **91**, 263601 (2003).
- [25] A. Mouchet, C. Eltschka, and P. Schlagheck, *Phys. Rev. E* **74**, 026211 (2006).
- [26] A. Bäcker, R. Ketzmerick, S. Lök, and L. Schilling, *Phys. Rev. Lett.* **100**, 104101 (2008).
- [27] B. Upcroft, Ph.D. thesis, The University of Queensland, 2003.
- [28] J. Fórtagh and C. Zimmermann, *Rev. Mod. Phys.* **79**, 235 (2007).
- [29] Note that this value is exact only in the limit of an unperturbed system.
- [30] R. Luter and L. E. Reichl, *Phys. Rev. A* **66**, 053615 (2002).
- [31] V. Averbukh, S. Osovski, and N. Moiseyev, *Phys. Rev. Lett.* **89**, 253201 (2002).
- [32] F. Grossmann, T. Dittrich, P. Jung, and P. Hänggi, *Phys. Rev. Lett.* **67**, 516 (1991).
- [33] B. P. Holder and L. E. Reichl, *Phys. Rev. A* **72**, 043408 (2005).
- [34] M. Wilkinson, *J. Phys. A: Math. Gen.* **20**, 635 (1987).
- [35] M. Abramowitz and I. Stegun (eds.), *Handbook of Mathematical Functions* (Dover, London, 1972).
- [36] T. Geisel, G. Radons, and J. Rubner, *Phys. Rev. Lett.* **57**, 2883 (1986).
- [37] R. Ketzmerick, L. Hufnagel, F. Steinbach, and M. Weiss, *Phys. Rev. Lett.* **85**, 1214 (2000).
- [38] S. Lök, A. Bäcker, R. Ketzmerick, and P. Schlagheck, *Phys. Rev. Lett.* **104**, 114101 (2010).
- [39] P. Kruger, L. M. Andersson, S. Wildermuth, S. Hofferberth, E. Haller, S. Aigner, S. Groth, I. Bar-Joseph, and J. Schmiedmayer, *Phys. Rev. A* **76**, 063621 (2007).
- [40] F. Dalfovo, S. Giorgini, L. P. Pitaevskii, and S. Stringari, *Rev. Mod. Phys.* **71**, 463 (1999).
- [41] S. Wüster, B. J. Dąbrowska-Wüster, and M. J. Davis, *Phys. Rev. Lett.* **109**, 080401 (2012).
- [42] C. J. Pethick and H. Smith, *Bose-Einstein Condensation in Dilute Gases* (Cambridge University Press, Cambridge, 2002).
- [43] J. Estève, C. Gross, A. Weller, S. Giovanazzi, and M. K. Oberthaler, *Nature* **455**, 1216 (2008).
- [44] K. Maussang, G. E. Marti, T. Schneider, P. Treutlein, Y. Li, A. Sinatra, R. Long, J. Estève, and J. Reichel, *Phys. Rev. Lett.* **105**, 080403 (2010).
- [45] J. Söding, D. Guéry-Odelin, P. Desbiolles, F. Chevy, H. Inamori, and J. Dalibard, *Appl. Phys. B* **69**, 257 (1999).
- [46] A. L. Subaşı, S. Sevinçli, P. Vignolo, and B. Tanatar, *Phys. Rev. A* **79**, 063632 (2009).